

Entrainment in dry and moist thermals

G. R. Vybhav*

Engineering Mechanics Unit, Jawaharlal Nehru Centre for Advanced Scientific Research, Jakkur, Bengaluru 560064

S. Ravichandran†

Nordita, KTH Royal Institute of Technology and Stockholm University, Stockholm SE 10691

We study entrainment in dry thermals in neutrally and unstably stratified ambients, and moist thermals in dry-neutrally stratified ambients using direct numerical simulations (DNS). We find, in agreement with results of Lecoanet and Jeevanjee [J. Atmos. Sci. 76(12), 3785-3801, (2019)] that turbulence plays a minor role in entrainment in dry thermals in a neutral ambient for Reynolds numbers $Re \lesssim 10^4$. We then show that the net entrainment rate increases when the buoyancy of the thermals increases, either by condensation heating or because of an unstably stratified ambient. This is in contrast with the findings of Morrison et al. [J. Atmos. Sci. 78(3), 797-816, (2021)]. We also show that the role of turbulence is greater in these cases than in dry thermals and, significantly, that the combined action of condensation heating and turbulence creates intense small scale vorticity, destroying the coherent vortex ring that is seen in dry and moist laminar thermals. These findings suggest that fully resolved simulations at Reynolds numbers significantly larger than the mixing transition Reynolds number $Re = 10^4$ are necessary to understand the role of turbulence in the entrainment in growing cumulus clouds, which consist of a series of thermals rising and decaying in succession.

I. INTRODUCTION

General circulation models (GCMs) that are used to predict the weather and climate solve the Navier-Stokes equations for the evolution of the properties of the Earth's atmosphere. These calculations are computationally intensive, especially at high resolutions. With present computational resources, the resolutions that can be achieved in GCMs are such that neighbouring horizontal grid-points are separated by tens if not hundreds of kilometres [1]. While approaches like superparameterisation [2–4], as a step towards global cloud resolving models that would obviate cumulus parameterisation, have been proposed, these are too computationally expensive at present. Individual clouds and most cloud systems, therefore, exist within a single grid box in current GCM simulations, and the processes occurring in clouds have to be parameterised.

Among the processes in clouds that need to be parameterised, the mixing of the fluid in the rising cloud with the ambient atmospheric air is the most important, since this controls the amounts of water substance in the cloud. The mixing process by which ambient fluid becomes part of the cloud flow is termed ‘entrainment’, and the process by which fluid leaves the cloud flow is termed ‘detrainment’. The parameterisation of entrainment in growing cumulus clouds has proved to be among the hardest problems to tackle in the general circulation models used today, since model outputs (e.g. the climate impact or regional rainfall patterns) depend sensitively on the entrainment parameterisation [5].

The most common approach adopted in parameterising entrainment in cumulus clouds is to model (ensembles of) these clouds as one of a few types of basic flow [5], typically plumes or thermals. (A review of other more recent approaches to modelling cumulus entrainment may be found in [1].) A steady state plume model for an ensemble of cumulus clouds is the most common model used in GCMs today [1, 5, 6], despite the evidence from airborne measurements as well as large eddy simulations (LES) that cumulus clouds more often resemble a series of thermals [7–16]. (See also Ref. [17] where observations and LES are found to disagree about whether shallow cumulus clouds show predominantly ‘bubble-like’ or ‘plume-like’ behaviour.) Cumulus convection can therefore be thought of as a succession of thermals, each rising further than its predecessor, entraining and mixing with the ambient air, and decaying. Understanding the fluid dynamics of thermals, therefore, may help improve the modelling of cumulus entrainment.

Laboratory experiments of (dry) thermals have been undertaken beginning in the 1950s [18–22], and have informed the understanding of entrainment. Studies using direct numerical simulations (DNS) of the entrainment in

* vybhav@jncastr.ac.in

† ravichandran@su.se

dry thermals are relative rare [e.g. 23, hereafter LJ19] and [24]. LJ19 show from DNS of laminar and turbulent dry thermals at two Reynolds numbers differing by a factor of 10 that the entrainment coefficients only differ by about 20%. They argue, following [19] that entrainment in dry thermals is driven not by turbulence but by buoyancy.

The assumptions that enable the analysis in [23, 24] break down (see section III) when the thermals are influenced not only by their initial buoyancy but also by off-source heating by condensation, as occurs in atmospheric clouds. The entrainment in such thermals naturally occurring in a moist convecting atmosphere has been studied in cloud-resolving simulations and LES [e.g. 10, 12, 13, 15, 16, 25]. Morrison et al. [26] study individual moist thermals using axisymmetric and 3D large eddy simulations (LES). In the initial few diameters from release, the authors find, moist thermals entrain less than dry thermals. After the initial stages, the entrainment rates in moist and dry thermals are indistinguishable. These results, as the authors note, are in contrast to earlier findings by the same authors and others that moist thermals do not grow in size [10, 12]. We also note that the axisymmetric and LES results in [26] seem to disagree about whether moist entrainment is the same as or different from dry entrainment in the initial stages (see, e.g. their figure 13 compared to their figures 3 and 5), with (noisy) LES results finding no difference between dry and moist thermals.

Here, we aim to definitively answer the question of whether moist thermals indeed entrain ambient fluid at rates different from dry thermals. To this end, we perform direct numerical simulations (DNS) resolving the smallest scales of the flow in thermals rising, studying cases with moist thermodynamics as well as with unstable ambient stratification.

The rest of the paper is organised as follows. In section II, we describe the geometry of the problem we study, and write down the governing equations in nondimensional form. We then list the controlling parameters and the initial and boundary conditions. We also briefly describe the numerical solver used to perform the DNS. In section III, we outline the theoretical arguments of LJ19 and list the cases we study to examine when these arguments break down. In section IV, we present results from the cases listed and discuss these results in light of earlier results in the literature. We conclude in section V.

II. GOVERNING EQUATIONS AND NUMERICAL METHOD

Our domain is a three-dimensional cuboidal volume with dimensions (L_x, L_y, L_z) in the three space directions. The horizontal directions are x and y , and gravity (of constant magnitude g) points in the $-z$ direction. We make the Boussinesq approximation [27], so that the fluid velocity \mathbf{u} is incompressible. The ambient temperature T_∞ is a function of the height z , and water vapour at a (constant) relative humidity s_∞ exists in the ambient; since the saturation vapour pressure is a steeply varying function of the temperature, the ambient vapour mixing ratio $r_{v,\infty}$ decreases rapidly with height.

The governing equations are the Navier-Stokes equations subject to the incompressibility condition, and advection-diffusion equations for the temperature and vapour and liquid mixing ratios. We nondimensionalise these equations using the initial temperature anomaly ΔT as the scale for temperature differences, the diameter of the thermal b_0 as the length scale, the buoyancy velocity $U_b = (b_0 g \Delta T / T_0)^{1/2}$ as the velocity scale, and the saturation mixing ratio $\tilde{r}_{s,0} = \tilde{r}_s(T_0)$ at the temperature T_0 as the scale for water quantities. The nondimensional equations become

$$\frac{D\mathbf{u}}{Dt} = -\nabla p + \frac{1}{Re} \nabla^2 \mathbf{u} + B \hat{e}_z, \quad (\text{II.1})$$

$$\nabla \cdot \mathbf{u} = 0, \quad (\text{II.2})$$

$$\frac{D\theta}{Dt} = \frac{1}{Re} \nabla^2 \theta + L_2 C_d + w (\Gamma_0 - \Gamma_u), \quad (\text{II.3})$$

$$\frac{Dr_v}{Dt} = \frac{1}{Re} \nabla^2 r_v - C_d, \quad (\text{II.4})$$

$$\frac{Dr_l}{Dt} = \frac{1}{Re} \nabla^2 r_l + C_d, \quad (\text{II.5})$$

where $\mathbf{u} = (u, v, w)$ is the fluid velocity, p is the dynamic pressure,

$$\theta = \frac{T - T_\infty}{\Delta T} \quad (\text{II.6})$$

is the temperature and the normalised vapour and liquid mixing ratios are $r_v = \tilde{r}_v / \tilde{r}_{s,0}$ and $r_l = \tilde{r}_l / \tilde{r}_{s,0}$ respectively. Quantities without the $\tilde{\cdot}$ are $O(1)$, since they are normalised using $\tilde{r}_{s,0}$. Similar equations have been used in [e.g.

Case	$L_x \times L_y \times L_z$	N_x, N_y, N_z	dt	Re	s_∞	$\Gamma_u - \Gamma_0$
DNL	$14^2 \times 28$	$384^2 \times 768$	0.002	630	0	0
DNT	$14^2 \times 28$	$768^2 \times 1536$	0.002	6300	0	0
DNT12	$14^2 \times 28$	$1024^2 \times 2048$	0.001	12600	0	0
MNL	$14^2 \times 28$	$768^2 \times 1536$	0.002	630	0.8	0
MNT	$14^2 \times 28$	$1024^2 \times 2048$	0.0015	6300	0.8	0
DUL	$12^2 \times 24$	$768^2 \times 1536$	0.002	630	0	-0.02
DUT	$12^2 \times 24$	$1024^2 \times 2048$	0.0015	6300	0	-0.02

Table I: List of cases presented, along with the domain size, resolution, and time step used in the simulations. These values are all nondimensional (see text). Note that the term $\Gamma_u - \Gamma_0$ is the nondimensional Brunt-Väisälä frequency. The Prandtl (Pr) and Schmidt (Sc) numbers are taken to be unity (close to atmospheric values). The grid resolutions chosen resolve the smallest scales for the respective cases. We run all the simulations until the thermal hits the boundary at $z = L_z$. The letters in the abbreviations stand for D: dry, M: moist, N:neutral, U:unstable, L:laminar and T:turbulent, with the 12 denoting $Re = 12600$.

28, 29]. The nondimensional Reynolds number is Re (defined in equation II.9), and the Prandtl and Schmidt numbers are implicitly assumed to be equal to unity. The nondimensional dry adiabatic lapse rate is Γ_u and the lapse rate in the ambient is Γ_0 (see table I). The thermodynamic constant L_2 is defined in equation II.10. Thus, the buoyancy

$$B = \theta + r_0 (\chi(r_v - r_{v,\infty}) - r_l), \quad (\text{II.7})$$

where $r_0 = \tilde{r}_{s,0}/(\Delta T/T_0)$ is a density ratio and $\chi = M_a/M_w - 1$ is derived from the ratio of molecular masses of air (M_a) and water vapour (M_w); the nondimensional condensation rate

$$C_d = \frac{1}{\tau_s} \left(\frac{r_v}{r_s} - 1 \right), \quad (\text{II.8})$$

where the local normalised saturation vapour mixing ratio $r_s \equiv \tilde{r}_s/\tilde{r}_{s,0} = \exp(L_1(\theta - \Gamma_0 z))$, and L_1 is a constant defined below; and the buoyancy and condensation rate are both functions of the local values of (θ, r_v, r_l) . The timescale for condensation or evaporation, τ_s , is a function of droplet size and liquid water mixing ratio, and, when τ_s is large, variations of τ_s can be important [see, e.g. 29]. Here, we assume that the droplets making up the liquid content r_l are very small, so that $\tau_s \ll 1$ and the system is always close to equilibrium. The governing parameters are the Reynolds number

$$Re = \frac{U_b b}{\nu}, \quad (\text{II.9})$$

and the ambient lapse rate Γ_0 and the ambient relative humidity s_∞ . The thermodynamic constants

$$L_1 = \frac{L_v \Delta T}{R_v T_0^2}; \text{ and } L_2 = \frac{L_v \tilde{r}_{s,0}}{C_p \Delta T} \quad (\text{II.10})$$

and the saturation mixing ratio $\tilde{r}_{s,0}$ are fixed when the temperature T_0 at the initial height z_0 and the temperature scale ΔT are chosen. We choose $T_0 = 300\text{K}$ and $\Delta T = 10\text{K}$, giving $L_1 \approx 0.58$ and $L_2 \approx 4.8$ and the saturation mixing ratio $\tilde{r}_{s,0} = 0.02$. We also choose a length scale $b = 100\text{m}$, such that the nondimensional dry adiabatic lapse rate $\Gamma_u = 0.098$. These values are typical of cumulus clouds in the tropics. Note that this means that the viscosity in our problem (equation II.9) is artificially large. We will, however, only report our results in nondimensional terms. We study the evolution of dry thermals in dry-unstably stratified and moist thermals in dry-neutrally (i.e. moist-unstably) stratified ambients. A list of the cases studied is given in table I.

Equations II.1 - II.5 are solved using the finite volume solver *Megha-5*, which uses second-order central differences in space and a second-order Adams-Bashforth timestepping scheme. Simple open flow boundary conditions [30] are imposed at the boundaries at $x = \pm L_x/2$, $y = \pm L_y/2$ and $z = L_z$, while the lower boundary at $z = 0$ is no-slip. The solver has been extensively validated and used in studies of free-shear flows, flows with moist thermodynamics, and combinations thereof [29, 31–34], and we refer readers to these earlier published works for details of the implementation.

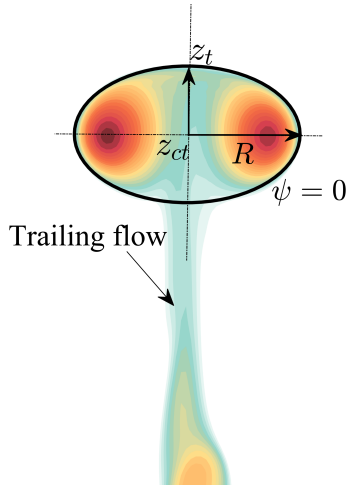


Figure 1: A typical (dry) thermal in our simulations, with the filled contours representing a typical distribution of the temperature θ coloured logarithmically. The radius of the thermal R is defined as the distance measured from the axis of symmetry ($r = 0$) to the widest location of the curve $\psi = 0$. The location of the centroid of the thermal z_{ct} is defined in Appendix A. The vertical locations of maximum radius and centroid of the thermal do not, in general, coincide. The thermal top height (z_t) is defined as the location of the steepest gradient of the azimuthally averaged temperature. The volume of the thermal is taken to be the volume bounded by the dividing streamline $\psi = 0$ in a frame of reference moving with the velocity w_{th} of the thermal (see section II B in the text). The maximum flow velocity in the region identified as the thermal is labelled w_{max} . The trailing flow suggests detrainment, which is small for dry thermals (see LJ19), but larger for moist thermals.

A. Initial Conditions

The thermal is initialised as a spherical patch with $\theta = 1$ and $r_v = s_\infty r_s(\theta = 0, z)$, so that the temperature in the thermals is greater than the local ambient temperature, and the vapour mixing ratio equal to the ambient value. The initial velocity is zero. We set $z_0 = 1.5$ in all cases reported here; the choice of z_0 does not affect our results. In both the laminar simulations at $Re = 630$ and the turbulent simulations ($Re = 6300$), noise is added to the initially spherical patch. We find, as in LJ19, that simulations with different instantiations of noise can produce significantly different results. Our results are therefore ensemble-averages over 5 runs at the same parameters for the turbulent simulations; for the laminar simulations where the effects of noise are smaller, we do not perform ensemble averages. Larger ensembles produced similar results, and we have verified that the type of noise used does not affect the results: Gaussian and uniformly distributed white noise lead to the same average results.

B. Tracking of thermals

The *net* entrainment rate is calculated from the rate of change of the volume V of the thermal,

$$\epsilon_{net} = \frac{1}{V} \frac{dV}{dz}. \quad (\text{II.11})$$

For a dry spherical thermal, ϵ_{net} can be written down analytically [see 24]. In order to find this rate numerically for a thermal of arbitrary shape, the volume of the thermal has to be consistently defined. Several methods have been used in the literature. In our simulations, we track the thermals as in, e.g., [10, 23, 26], as described presently.

We first calculate the velocity at which the thermal rises vertically by calculating the time derivative of the location of the centroid z_{ct} of the thermal. Then, in a frame of reference moving with the thermal, we compute the azimuthally averaged flow velocity and thus the streamfunction ψ of the flow. The volume bounded by the dividing streamline $\psi = 0$ is assumed to be the volume of the thermal, as shown in figure 1. The *net* entrainment rate is then calculated using equation II.11. These calculations are detailed in Appendix A.

Since the entrainment rate thus defined is expected to vary as $1/R$, we also define the entrainment efficiency

$$e = \epsilon_{net} R \quad (\text{II.12})$$

III. THEORETICAL PRELIMINARIES

Since there are several governing nondimensional parameters and combinations of ambient conditions, we outline our approach to studying entrainment in thermals, and our reasons for studying the specific cases reported in section IV.

For completeness, we briefly recount the arguments of LJ19 following Turner [35]. Buoyant vortex rings are known to expand in a flow and, since thermals ‘spin up’ into vortex rings, the impulse

$$I = \frac{1}{2}\rho \int \mathbf{r} \times \boldsymbol{\omega} dV \quad (\text{III.1})$$

of a dry thermal may be written as the impulse of a vortex ring with circulation

$$\Gamma = \int \omega_\phi dr dz, \quad (\text{III.2})$$

where the integral is over the cross-sectional area of the vortex ring, and radius R , giving

$$I = \pi\rho\Gamma R^2, \quad (\text{III.3})$$

where ρ is the fluid density. Note that the symbol Γ (no subscript) is used for the circulation, and $\Gamma_{0,d}$ are used for the nondimensional (constant, imposed) ambient lapse rates. Since the impulse of a flow can only increase by the action of an external force, here the buoyancy of the thermal, this impulse increases with time at a rate

$$\frac{dI}{dt} = \pi\rho R^2 \frac{d\Gamma}{dt} + \pi R^2 \Gamma \frac{d\rho}{dt} + \pi\rho\Gamma \frac{dR^2}{dt} = F, \quad (\text{III.4})$$

where F is the volume-integrated buoyancy force on the thermal. In dry thermals, F is nearly constant since detrainment is about two orders of magnitude smaller than entrainment. Furthermore, since Γ is also constant for vortex rings, and ρ is constant (under the Boussinesq approximation in a neutrally stratified ambient), the dR^2/dt term alone has to balance the buoyancy force term on the right hand side and we have

$$\pi\Gamma\rho \frac{dR^2}{dt} = F. \quad (\text{III.5})$$

Since the preceding arguments are independent of the level of turbulence, entrainment in dry thermals cannot be turbulent in nature. As mentioned in section I, LJ19 show that increasing the Reynolds number from $Re = 630$ to $Re = 6300$ changes the entrainment rate by only about 20%. Further evidence for the role of buoyancy in entrainment in dry thermals is found in [24] where switching off buoyancy also reduces the entrainment rate to about 1/3rd of its value.

Clearly, this analysis breaks down [see, e.g., the arguments in 26] if either of the first two terms in the expansion of dI/dt in equation III.4 is nonzero. This can occur

(i) by the off-source heating of the thermal by condensation which (a) generates vorticity inside the thermal so the first term is nonzero; and (b) changes the density of the thermal, so the second term can be nonzero.

(ii) by detrainment which in dry thermals is very small compared to entrainment, but could be significant in moist thermals, thus changing the density ρ of the thermal.

(iii) when the (effective) radius of the vortex core is no longer small compared to the radius R of the vortex ring, so that the definition of the impulse equation III.3 in terms of the vortex strength Γ (eq. III.2) is no longer accurate [see, e.g., the discussion in 24]. LJ19 comment that in their simulations at the higher $Re = 6300$, this requirements are not met as well as in their laminar simulations. This is also evident in our turbulent simulations at $Re = 6300$, as discussed in section IV A, where the thermals appear to become more elongated.

The terms in Eq. III.4 are explicitly computed in section IV E. We note, however, that under the Boussinesq approximation which we make here, the contributions due to changing density cannot strictly be computed. Density changes with altitude can be accommodated using the anelastic approximation [36], while fully compressible simulations (such as in [26]) are needed to account for local density changes.

To test possibilities (i) and (ii), we study the evolution of moist thermals in a (dry-) neutrally stratified ambient (section IV B) and the evolution of a dry thermal in an dry-unstably stratified ambient (section IV C). Regarding the role of turbulence (iii), we note that in general, shear-dominated (buoyancy or momentum-driven) flows are known to undergo a transition to a higher mixing rate for a large scale Reynolds number $Re \geq \mathcal{O}(10^4)$ [37], and the Reynolds number in LJ19 is smaller than this mixing transition Reynolds number. If the assumption that the vortex core radius is small no longer holds for sufficiently large Reynolds numbers, turbulence could play a greater role in the entrainment. We test this notion by studying a dry thermal at a Reynolds number of $Re = 12,600 > 10^4$ (section IV D).

A possible source of error in this exercise is the inconsistent definition of the radius R . LJ19 (consistently) define R to be the radius of the *vortex ring* and use this in their calculations; whereas Morrison et al. [26], while defining R to be radius of the vortex ring, use the radius of the thermal in their calculations. We examine the results of this switch in IV E (see Fig. 17)

IV. RESULTS AND DISCUSSION

A. Dry thermals in a dry-neutral ambient

We begin with results from simulations of dry thermals in a neutral ambient. Our results are in good agreement with those of [23], and therefore serve both as validation of our methods of numerical analysis as well as independent verification of the results of LJ19.

Figure 2 shows the evolution of laminar ($Re = 630$) and turbulent ($Re = 6300$) dry thermals in our simulations. These may be compared with Figure 1 in LJ19. Vortex rings with cores where the temperature contrast is concentrated are seen for both laminar and turbulent cases [see, e.g., 38]. We note the differences in shape between the laminar and turbulent cases, as well as the fact that the tails in the turbulent case are more prominent (and hence that the detrainment is marginally larger), which are also in agreement with LJ19.

Our results are thus broadly consistent with LJ19. The net entrainment rate obeys the relation $\epsilon \sim R^{-1}$ for $R < 2$. The values for laminar and turbulent thermals differ by less than 10%, whereas LJ19 report a 20% difference. Despite this, it is clear that the entrainment rate is not a strong function of Re at least for $Re < 10^4$ [37].

The net entrainment ϵ_{net} and entrainment efficiency $e = \epsilon_{net}R$ are plotted in figure 3(a,b) respectively. These are comparable to Figures 5 and 7 in LJ19. The entrainment efficiency remains essentially constant for $z_{ct} < 17$ for both laminar and turbulent thermals. There is a slow decrease in entrainment efficiency above $z_{ct} > 17$, also noted by LJ19, perhaps because of boundary effects.

The evolution of the thermal location, the maximum flow velocity in the thermal, the thermal radius and the thermal volume are plotted in figures 14 (a-d) respectively in section IV D, and the curves for $Re = 630$ and $Re = 6300$ therein may be compared with Figure 4 in LJ19.

B. Moist thermals in a dry-neutral ambient

Having validated our numerical method and analysis on dry thermals, we apply the same methods to moist thermals in a dry-neutrally stratified ambient.

Laminar and turbulent moist thermals are initialised as described in section II A, and instantaneous slices of the temperature θ and azimuthally averaged liquid water mixing ratio r_l are shown in figures 4 and 5 respectively. Unlike dry thermals which take the form of vortex rings (section IV A), the laminar moist thermals develop a distinct ‘arrowhead’ shape which includes the vortex ring; in turbulent moist thermals, the coherent vortex ring and arrowhead shape are destroyed, and the flow features are small-scale (figures 6 and 7).

Condensation heating and the resulting increase of buoyancy in the MNL thermal leads to significantly larger values of the azimuthal vorticity (figure 6) compared to the DNL thermal (not shown). The other components of the vorticity are of much smaller magnitude in these laminar cases where the rings are coherent. In both dry and moist turbulent thermals, on the other hand, the flow is more isotropic and the different components of the vorticity are of similar magnitude, and we find that the combined action of condensation heating in concert with turbulence lead to maximal vorticity magnitudes $|\omega|$ 4 – 5 times larger in the MNT thermals than in the DNT thermals (figure 7).

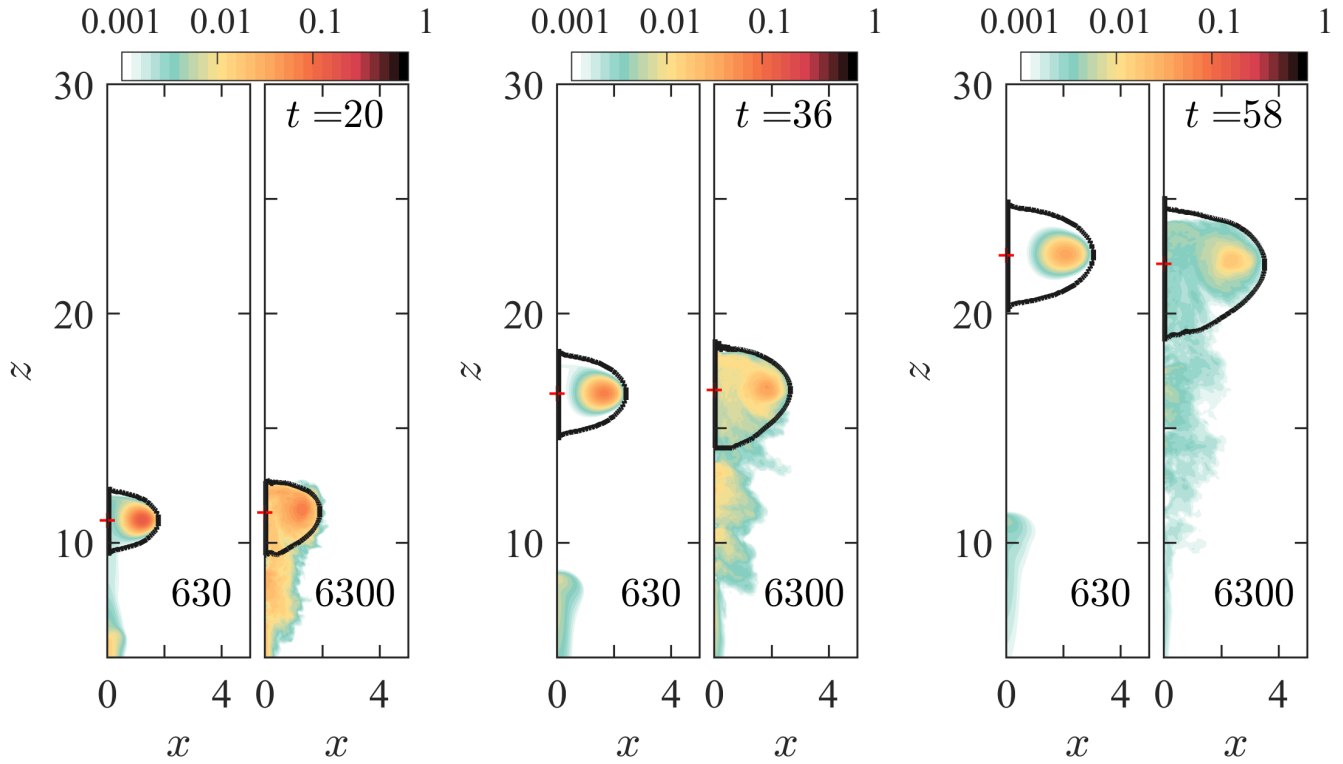


Figure 2: The azimuthally averaged temperature θ in laminar ($Re = 630$, left panels) and turbulent ($Re = 6300$, right panels) dry thermals in a neutrally stratified ambient at the times indicated. The thermals were initialised with the same level of noise. The colour maps are logarithmically scaled and the same for all three times shown. The laminar thermals have spun up into vortex rings as expected. The turbulent thermals are noticeably different in shape, with more diffuse cores and more prominent tails.

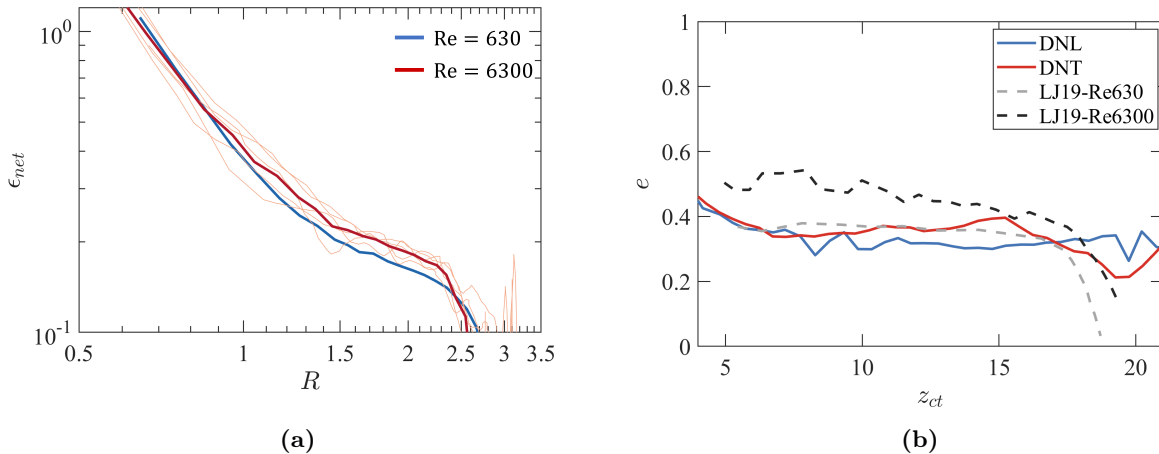


Figure 3: The (a) entrainment rate and (b) entrainment efficiency, defined in equations II.11 and II.12, for laminar (blue, $Re = 630$) and turbulent (red, $Re = 6300$) dry thermals in a neutral ambient ($\Gamma_0 = \Gamma_u$). The thin red lines are the five individual runs for the turbulent thermals with different instantiations of noise, while the average is plotted as a thick line.

In (b), the curves from LJ19 are also plotted for comparison. Turbulent entrainment rates are marginally higher than laminar entrainment rates, and the difference is smaller than in LJ19. There is a dip in the value of e after $z_{ct} > 16$, more pronounced in the turbulent cases, which is also seen in LJ19.

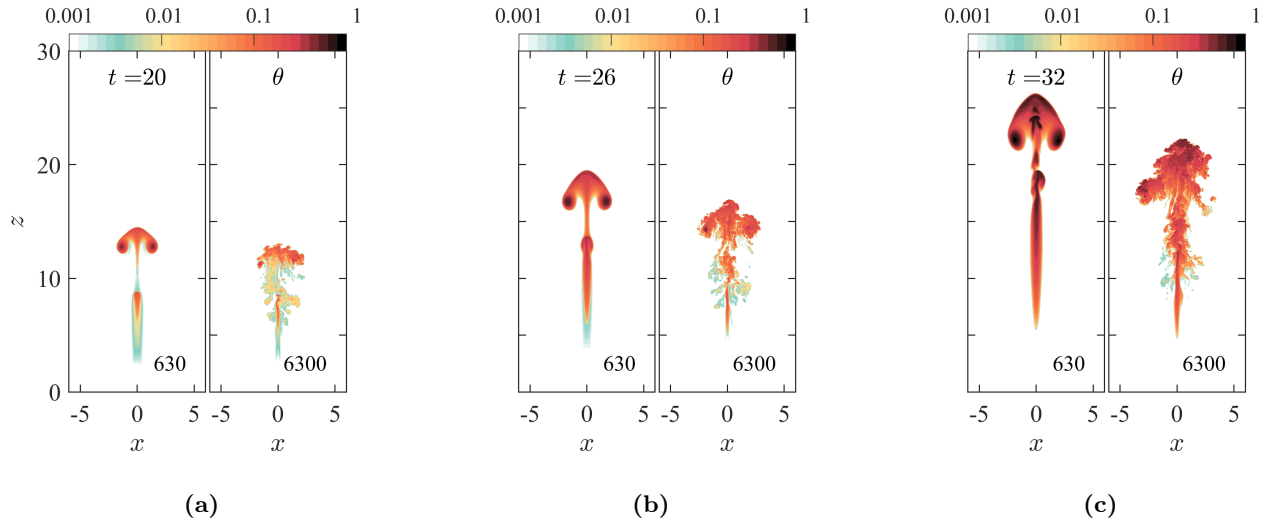


Figure 4: Instantaneous 2D slices at $y = 0$ of the temperature θ in laminar ($Re = 630$, left panels) and turbulent ($Re = 6300$, right panels) moist thermals at the times indicated. As in figure 2, a logarithmic colour scale is used. Laminar moist thermals assume a distinct ‘arrowhead’ shape where the vortex ring remains. See figure 8 for corresponding plots of the vertical velocity.

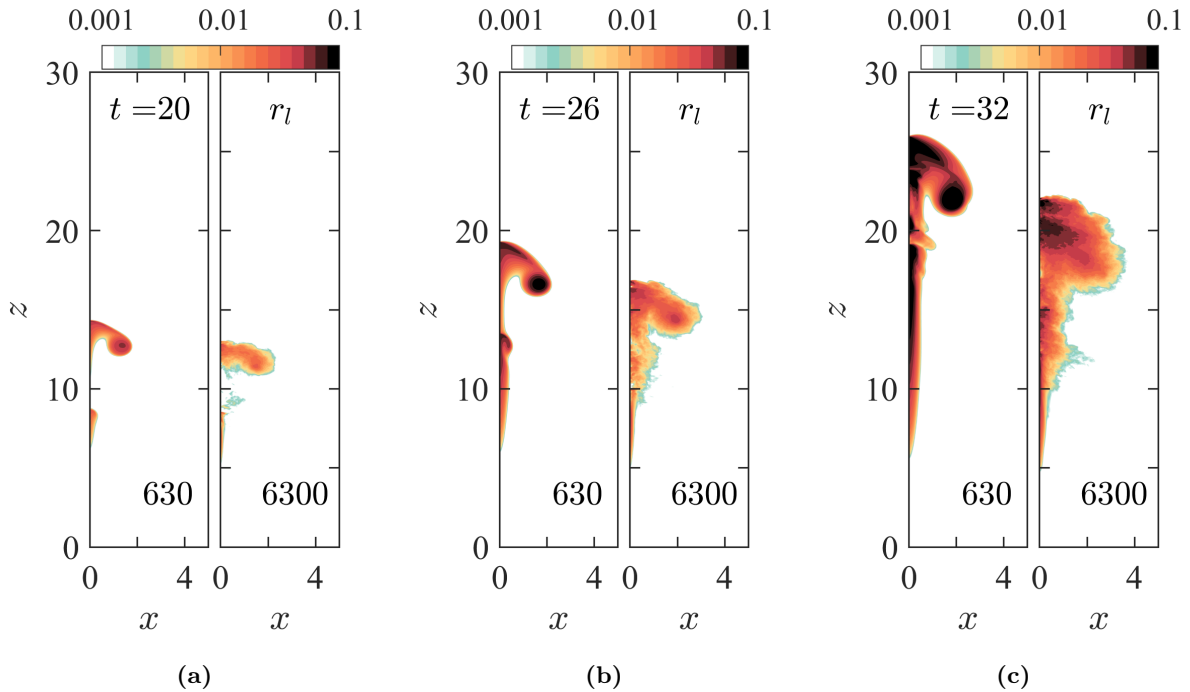


Figure 5: Azimuthally averaged liquid mixing ratio r_l for laminar ($Re = 630$, left panels) and turbulent ($Re = 6300$, right panels) moist thermals in a dry-neutrally stratified ambient at the same times as in figure 4. (a) initially, moist thermals behave similarly as dry thermals, forming vortex rings whose cores have large r_l in both laminar and turbulent cases. (b) these vortex rings morph into the ‘arrowhead’ shape with large r_l both in the vortex cores as well as the tip of the arrow.

(c) at $t = 32$, the distribution of r_l is very different in the laminar and turbulent cases; in the laminar thermal, large r_l values occur in the vortex ring as well as the thermal top, whereas the vortex ring is destroyed in the turbulent thermal and the maximum in r_l occurs only at the thermal top. Note that a logarithmic colour scale is used.

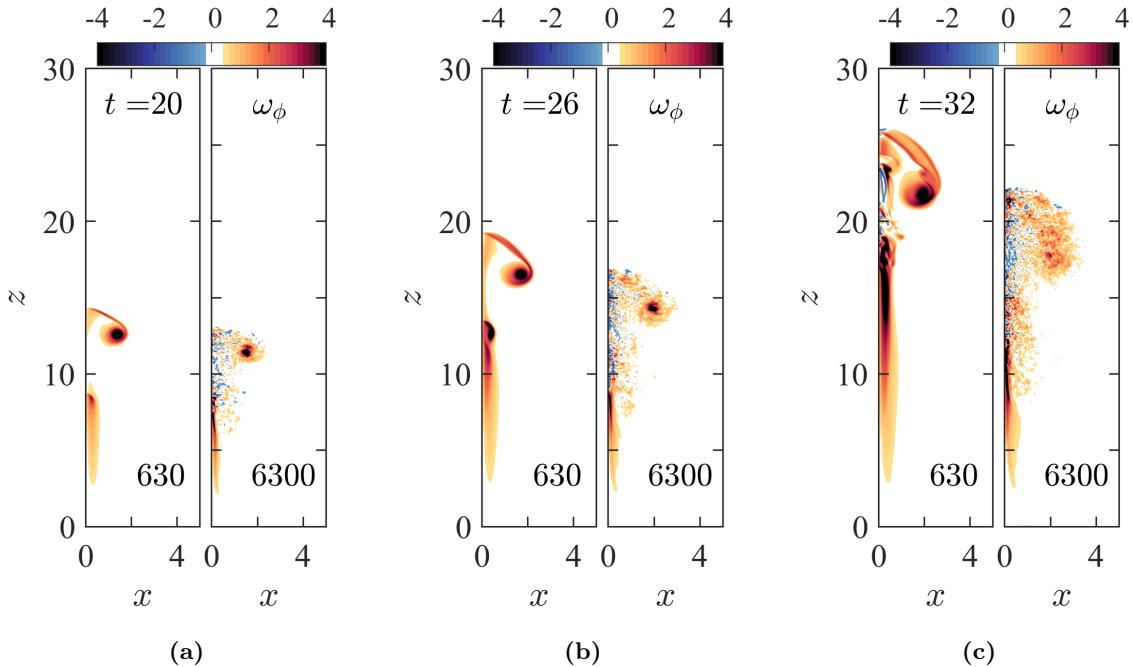


Figure 6: Azimuthally averaged azimuthal vorticity ω_ϕ for laminar ($Re = 630$, left panels) and turbulent ($Re = 6300$, right panels) moist thermals in a dry-neutral ambient at the same times as in figure 4. (a) The vorticity is initially concentrated in the vortex ring that forms. (b) The vorticity in the ring increases in the laminar thermal, while the ring becomes more diffuse in the turbulent thermal. (c) significant negative vorticity can be seen along the axis of symmetry in both laminar and turbulent thermals, and the vortex ring in the turbulent thermal is even more diffuse.

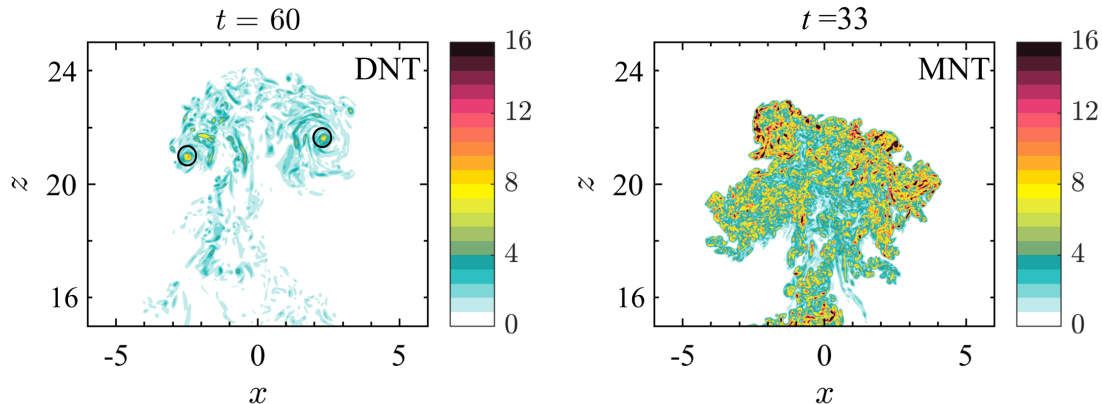


Figure 7: Vorticity magnitude ($|\omega| = \sqrt{\omega_x^2 + \omega_y^2 + \omega_z^2}$) in (a) DNT and (b) MNT thermals. The black circles in (a) denote the location of core of the vortex ring in the DNT thermal. In the MNT thermal in (b), the vortex ring has disintegrated and the vorticity is space-filling, and the maximum $|\omega|$ is ≈ 5 times higher than in (a).

Furthermore, the coherent vortex core present in the dry thermals (even for larger Re ; see Section IVD) is destroyed in the MNT thermal; thus, turbulence is a necessary but not sufficient condition for the destruction of the vortex ring and the emergence of intense small-scale vorticity in the flow. In highly turbulent flows, the magnitude of the vorticity fluctuations relative to the mean vorticity is known to increase with the flow Reynolds number as $\omega' \sim Re^{1/2}$ [e.g. 39], and our observations are consistent with this. Such small scale vorticity may be responsible for the crinkly edges seen in cumulus clouds [39]. This generation of intense small scale vorticity is also responsible for the smaller vertical mean velocities seen in plots of the vertical velocity w in figure 8.

From figures 4 – 8, we see, as also reported in Ref. [26], that a condensing thermal in a dry-neutrally stratified ambient is highly unstable and leads to large vertical velocities; and thus the effective Reynolds numbers in the turbulent moist thermal are a factor 4 – 5 larger than the nominal $Re = 6300$.

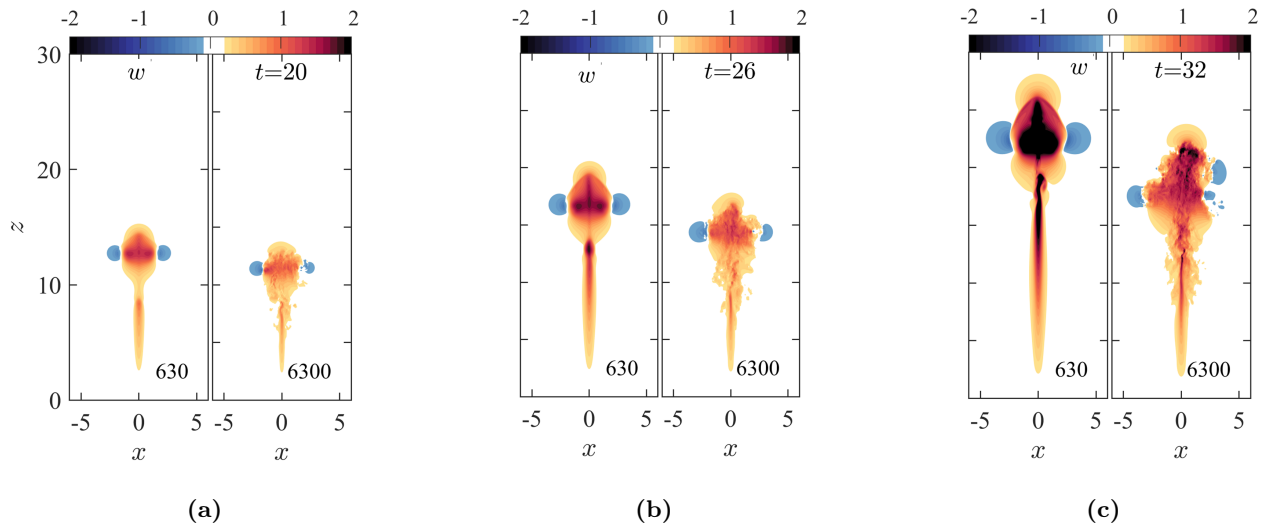


Figure 8: Instantaneous 2D slices at $y = 0$ of the vertical velocity w in laminar ($Re = 630$, left panels) and turbulent ($Re = 6300$, right panels) moist thermals at the same times as in figure 4. The vertical velocities for moist thermals are significantly higher than for dry thermals. (a) The flow is initially axisymmetric, with maximum velocities at the vortex rings. (b) As the thermal is heated by condensation, the laminar case retains its symmetry but the turbulent case can be seen to show departures from symmetry. Large velocities occur both in the rings and in thermal centre. (c) Velocities have increased significantly in both laminar and turbulent thermals. The laminar thermal continues to be axisymmetric and the vortex ring continues to become stronger, whereas the vortex ring is destroyed in the turbulent case. C.f. figures 4 and 6.

The location, maximum flow velocity, radius and volume of moist thermals are compared with dry thermals in figure 9. We see that the velocities in moist thermals are larger than the velocities in dry thermals by a factor of 2 – 3 whereas the buoyancy is larger by an order of magnitude (compare figures 2 and 4). This is consistent with the idea that the velocity scale is set by the square root of the buoyancy scale (see Sec. II).

We also find that moist thermals have *larger* volumes than the corresponding dry cases, that the thermal radii in the moist turbulent case are larger than the radii of dry thermals of the same nominal Re , and that in both dry and moist thermals, turbulence leads to larger thermal volumes and radii and smaller velocities. However, the influence of turbulence is significantly larger in moist thermals.

The larger entrainment rate in moist thermals is in contrast to the findings in Ref. [26] from axisymmetric and 3D LES that moist thermals have *smaller* volumes and radii than dry thermals. The reasons for this difference are unclear. Morrison et al. argue in Ref. [26] that the radial distribution of the heat added to the thermals (by condensation) results in the smaller entrainment in moist thermals in the initial stages (e.g. see their figure 6). We note, however, that the ‘arrowhead’ shape that laminar moist thermals take (figure 4) permits the same mechanism of outward expansion operant in dry thermals that is shown schematically in figure 9 of Ref. [26].

Similarly, the large increase of vorticity due to the action of (external) buoyancy addition has been noted in earlier numerical studies [e.g. 40], and is thought to be responsible for the increased mixing of the fluid inside the flow seen in Ref. [41]. These studies also report a *decrease* in entrainment attributed to the destruction of the coherent toroidal vortical structures due to the external heat addition, which we do not see. We instead find that laminar moist thermals rise faster than turbulent moist thermals, and grow to smaller radii and volumes (and therefore have smaller entrainment rates).

Entrainment in shear flows may occur through the action of large scale coherent structures (through ‘engulfment’), or intense small scale vortices (through ‘nibbling’), or a combination [42, 43]. The role of buoyancy in entrainment (LJ19 and Section IV A) suggests the former, while the fact that increased turbulence leads to greater entrainment in moist thermals suggests that the latter may not be negligible. The relative importance of these mechanisms (whether there is a transition beyond some critical Re , say) is a subject of ongoing study.

Turbulence is known to lead to increased scalar mixing *across* a shear layer [e.g. 44]. In clouds, this mixing of the saturated cloud parcel with the unsaturated ambient air can lead to evaporative cooling and a subsiding shell of colder fluid at the edges of the cloud [45]. This subsiding shell is richer in vapour than the ambient, and may subsequently be re-entrained into the cloud [25], thus altering the rate of dilution of the flow [46]. As a result, trailing thermals often encounter different properties from their predecessors which dissipated more quickly, which

is an important factor in the behaviour of thermal chains [16, 47].

We noted that due to the addition of buoyancy through condensation heating and the resulting increase in both their vertical velocity and radius, the turbulent moist thermals in figures 4–8 have effective Reynolds numbers 4–5 times larger than the nominal $Re = 6300$. In section IV C, we study the addition of buoyancy through unstable stratification instead of condensation heating.

Furthermore, in order to delineate the effects of buoyancy addition from the effects of turbulence, we study thermals with a nominal $Re = 12600$ in section IV D.

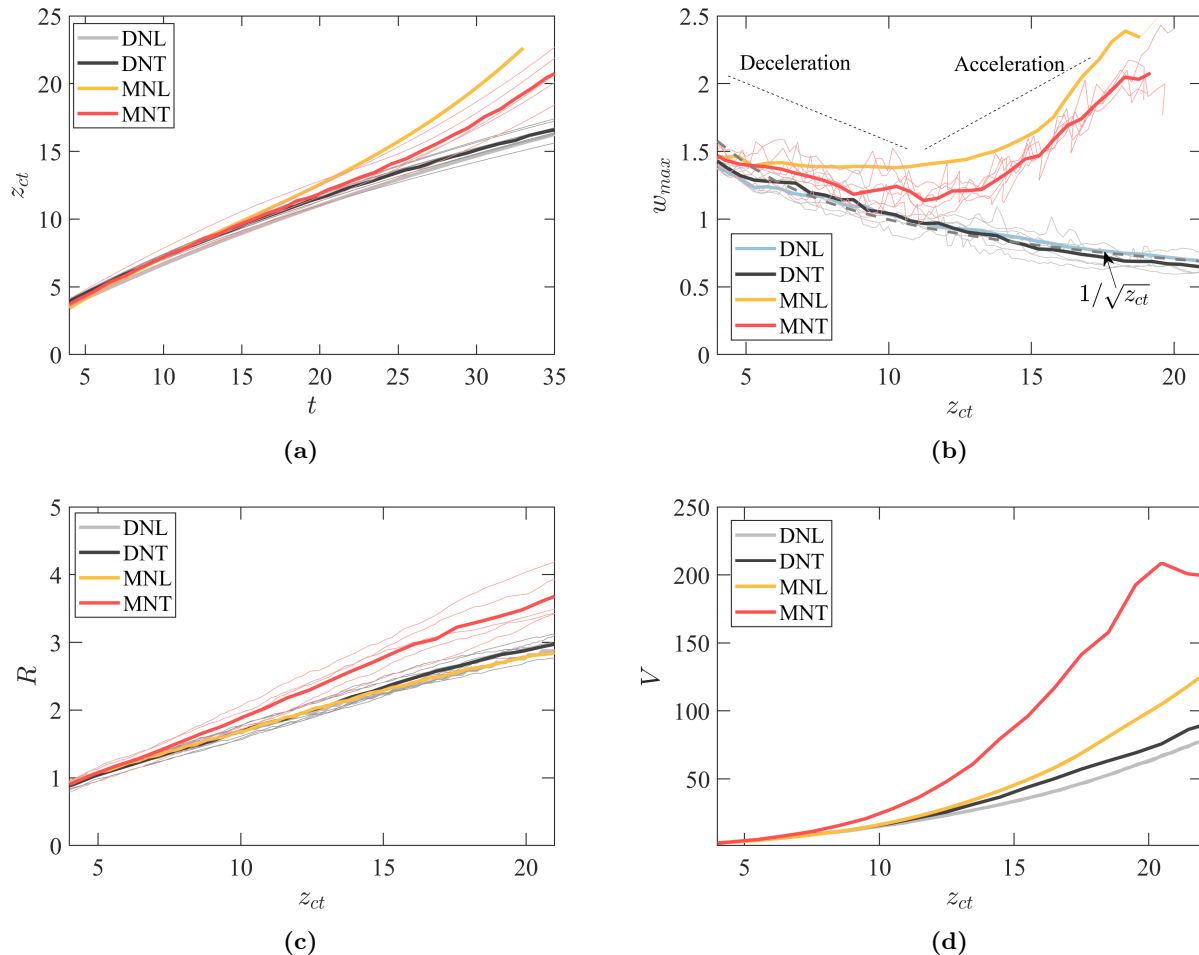


Figure 9: The (a) location z_{ct} , (b) maximum velocity w_{max} (c) radius R , and (d) volume V of laminar ($Re = 630$) and turbulent ($Re = 6300$) moist thermals in a (dry-) neutrally stratified ambient. The x-axis starts from four for all the sub figures. The curves for dry thermals in the same ambient are shown for comparison. In each case, individual runs are plotted as thin lines while ensemble averages are plotted as thick lines. Moist thermals begin to accelerate for $z_{ct} \gtrsim 10$ due to condensation heating and, as a result, grow to larger radii, have greater volumes and rise faster than dry thermals. It is worth noting that, even though the volumes of the moist thermals grow much faster than their dry counterparts, the radius of the moist laminar thermal grows similarly to the dry cases. This is due to a change in the shape of the thermal (see, e.g., figure 19; see also figure 15).

C. Dry thermals in a dry-unstable ambient

In moist thermals, the buoyancy of the thermal increases due to condensation heating. The buoyancy of the thermal can also increase if the ambient is unstably stratified, i.e. when the lapse rate in the ambient is greater than the dry adiabatic lapse rate. The evolution of θ and w for a dry thermal in an ambient with $\Gamma_0 - \Gamma_u = 0.02$ is shown in figures 10 and 11 respectively. We see that the flow resembles the starting plumes described by Turner [20], with heads that are thermals and plumes rising behind them. We note that the shape of the thermals in

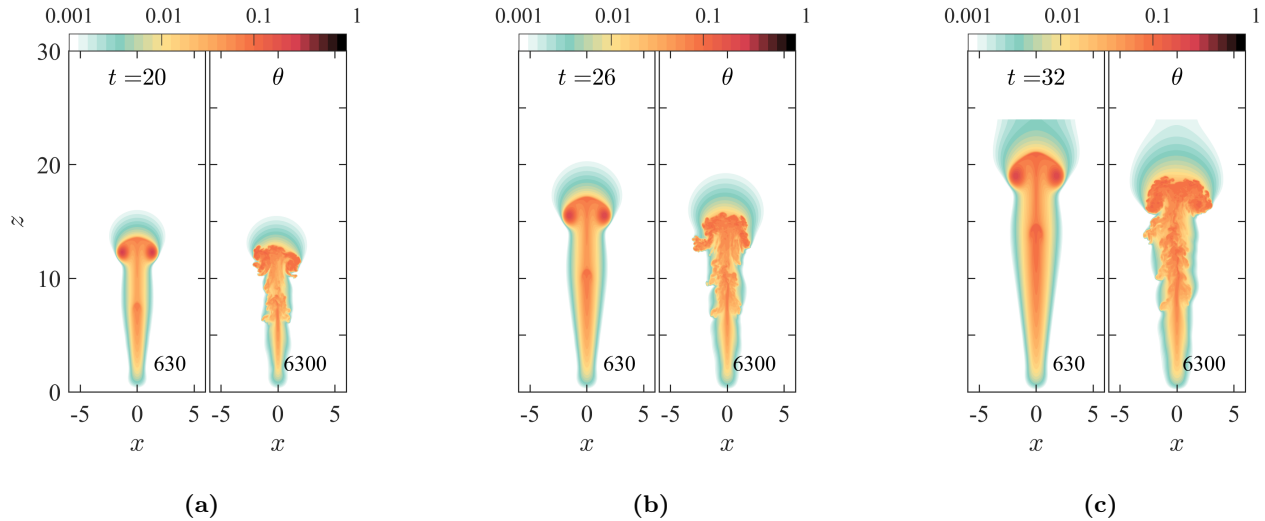


Figure 10: As in figures 2 and 4, but for dry thermals in an unstably stratified ambient.

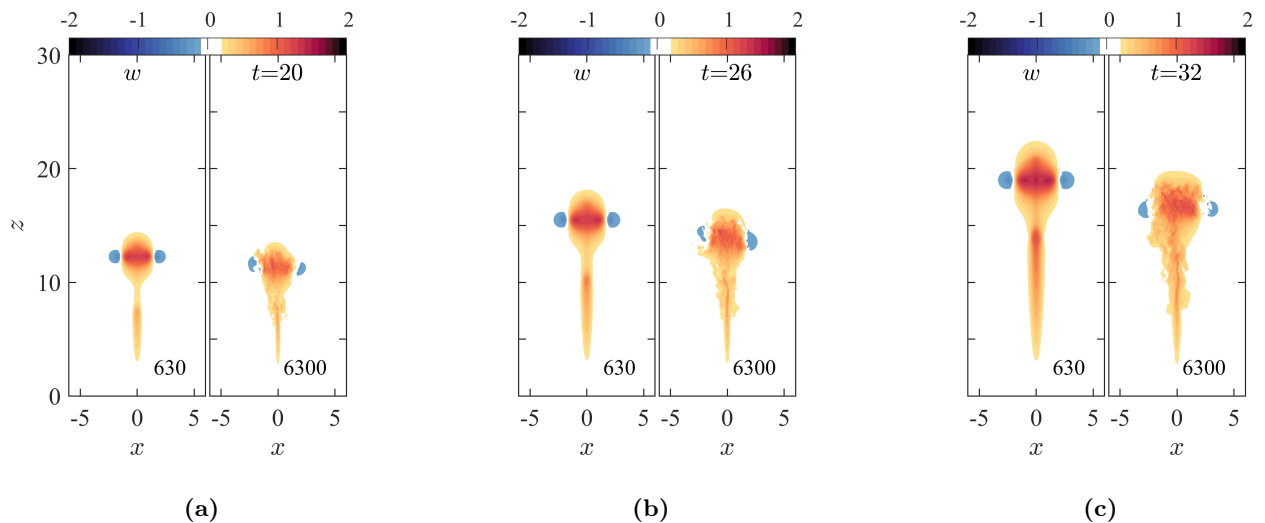


Figure 11: As in figure 8, but for dry thermals in an unstably stratified ambient.

figure 10 resembles the ‘arrowhead’ shape in figure 4. Since the ambient is inherently unstable, even small upward velocities that the ambient air in the wake of the thermal are amplified.

In figure 12, we compare the location, maximum flow velocity, radius and volume of dry thermals in unstably and neutrally stratified ambients. As in moist thermals (section IV B), the volume and radius (and velocity) of dry thermals in unstably stratified ambients increase with time faster than dry thermals in a neutrally stratified ambient. Furthermore, as in moist thermals, the influence of turbulence is larger in accelerating dry thermals than in dry thermals in a neutrally stratified ambient. Unlike in moist thermals, however, the arrowhead shape is not completely destroyed in turbulent dry thermals here.

D. Dry thermals in a dry-neutral ambient at $Re = 12600$

Figure 2 shows that turbulent dry thermals can evolve such that their vortex cores are not small, with vorticity in their interiors and that they detrain at larger rates. The spread of the vortex cores is greater for an even larger $Re = 12600$, as seen from the evolution in figure 13. In section III, we hypothesised that the spreading of the vortex

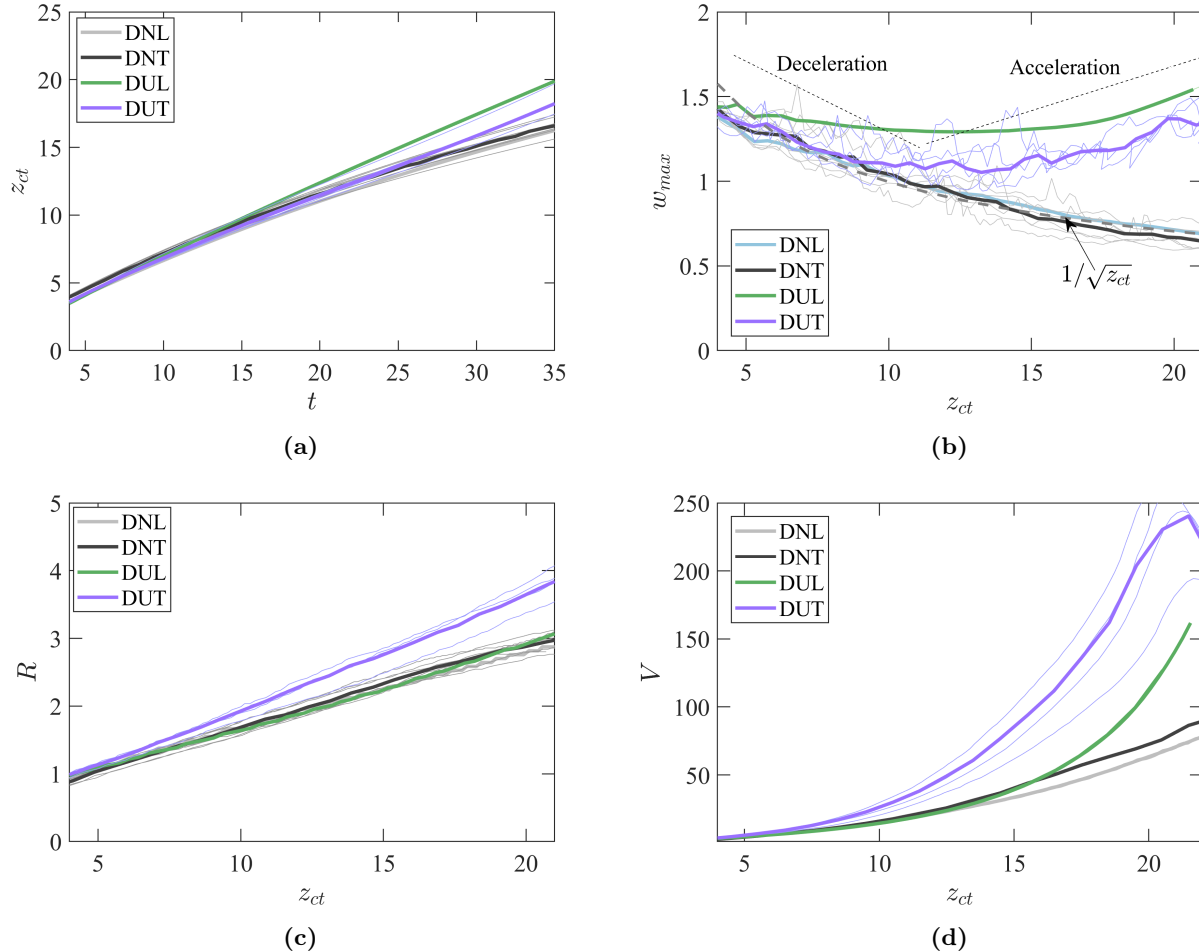


Figure 12: The (a) location z_{ct} , (b) vertical velocity w_{th} (c) radius R , and (d) volume V of laminar ($Re = 630$) and turbulent ($Re = 6300$) dry thermals in an unstably stratified ambient with $\Gamma_0 - \Gamma_u = 0.02$ compared with dry thermals in a neutrally stratified ambient. Similarly to moist thermals in a (dry-) neutrally stratified ambient, the accelerating thermals here rise faster, grow to greater radii, and have larger volumes than dry thermals in a neutrally stratified ambient. Also note that the laminar thermals rise faster but have smaller radii and volumes than the turbulent thermals. The changing shape of the thermal accounts for the increase in thermal volume in the laminar case even though the thermal radius evolves similarly to the dry thermals in a neutral ambient (c.f. 9).

core, (or even complete disintegration; see section IV B) may mean that at a sufficiently large Reynolds number, the entrainment could change significantly. However, our results at $Re = 12600$ are inconclusive. The mean values of entrainment rate and entrainment efficiency are approximately the same as those found for $Re = 6300$. We note that this is an imperfect test: while finding significant differences would have shown that turbulence plays a role, finding no differences does not rule out a role for turbulence, since the Reynolds number studied here is barely above the mixing transition Reynolds number of 10^4 .

The plots of thermal location, maximum velocity, radius and volume in figure 14 show that thermals at the higher Reynolds numbers rise at (slightly) smaller velocities, and that the thermal volume and radius increase faster for larger Re . The entrainment rates are therefore larger for larger Re . This is not a qualitative change, however, and simulations at Reynolds number much greater than 10^4 are therefore necessary to determine if the effects of turbulence are indeed small beyond the mixing transition.

E. Entrainment rate and entrainment efficiency

In sections IV A - IV D, we examined several cases of dry and moist thermals, and compared their evolution with the standard case of dry thermals in a neutrally stratified ambient. In figure 15, we plot the thermal volume as

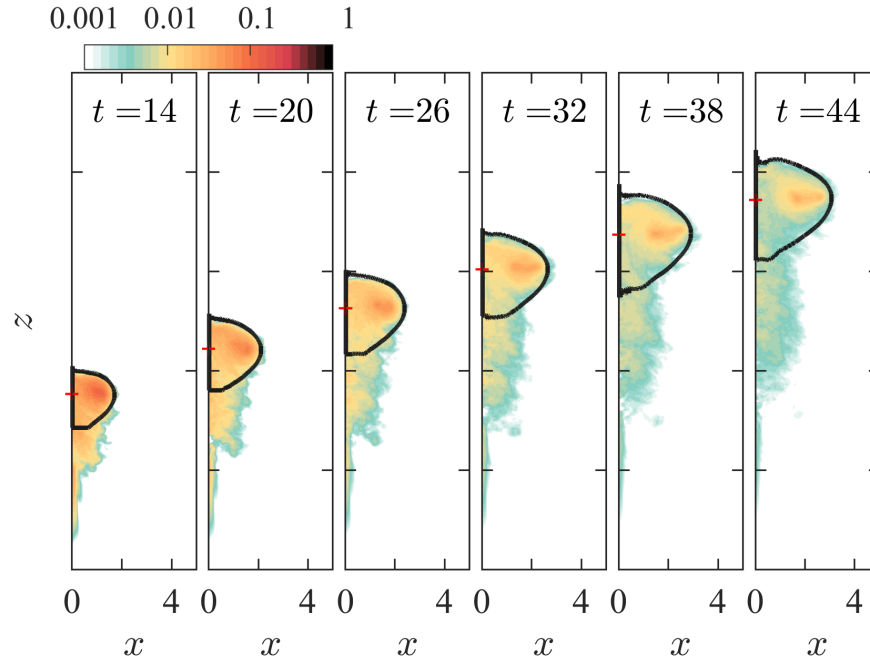


Figure 13: The evolution of a dry turbulent thermal at $Re = 12600$. The contour plots shows the aximuthally averaged temperature θ and as with other cases, the black line represent the thermal boundary. C.f. the laminar and turbulent ($Re = 6300$) cases in figure 2.

a function of the thermal radius, showing that $V \sim R^3$ and suggesting that the evolution of the thermals in all these cases is self-similar, and therefore that analytical or reduced-order models for the evolution of thermals may be possible.

Figures 9, 12 and 14 also show that thermals that have an external source of buoyancy—either condensation heating or an unstable ambient stratification—grow fastest in volume, and thus have the largest entrainment rates.

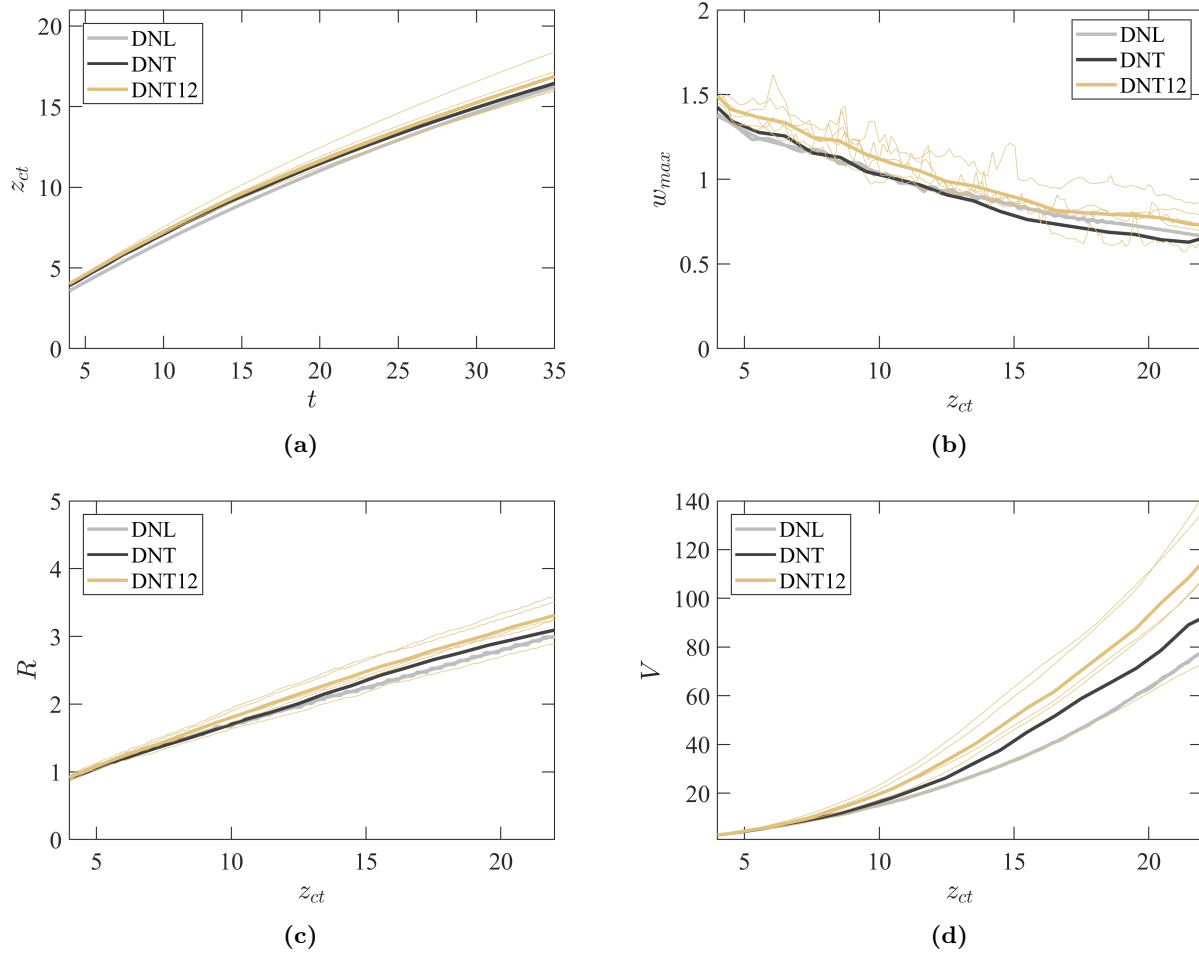


Figure 14: The (a) location z_{ct} , (b) maximum velocity w_{max} , (c) radius R and (d) volume V of a laminar dry thermal ($Re = 630$) and turbulent dry thermals ($Re = 6300$ and $Re = 12600$) in a neutrally stratified ambient. In the turbulent case, curves for individual runs at $Re = 6300$ (thin grey lines) and $Re = 12600$ are plotted along with the ensemble average.

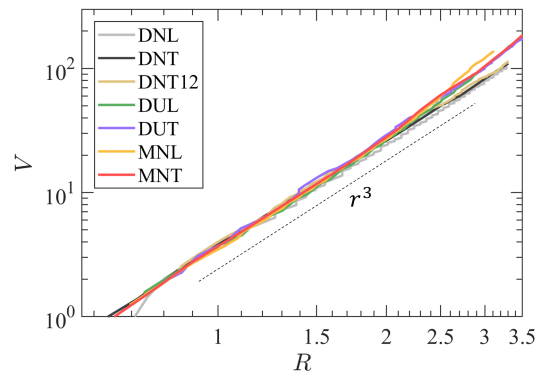


Figure 15: As thermals rise, the volume scales with the thermal radius as $V \propto R^3$, suggesting self-similarity.

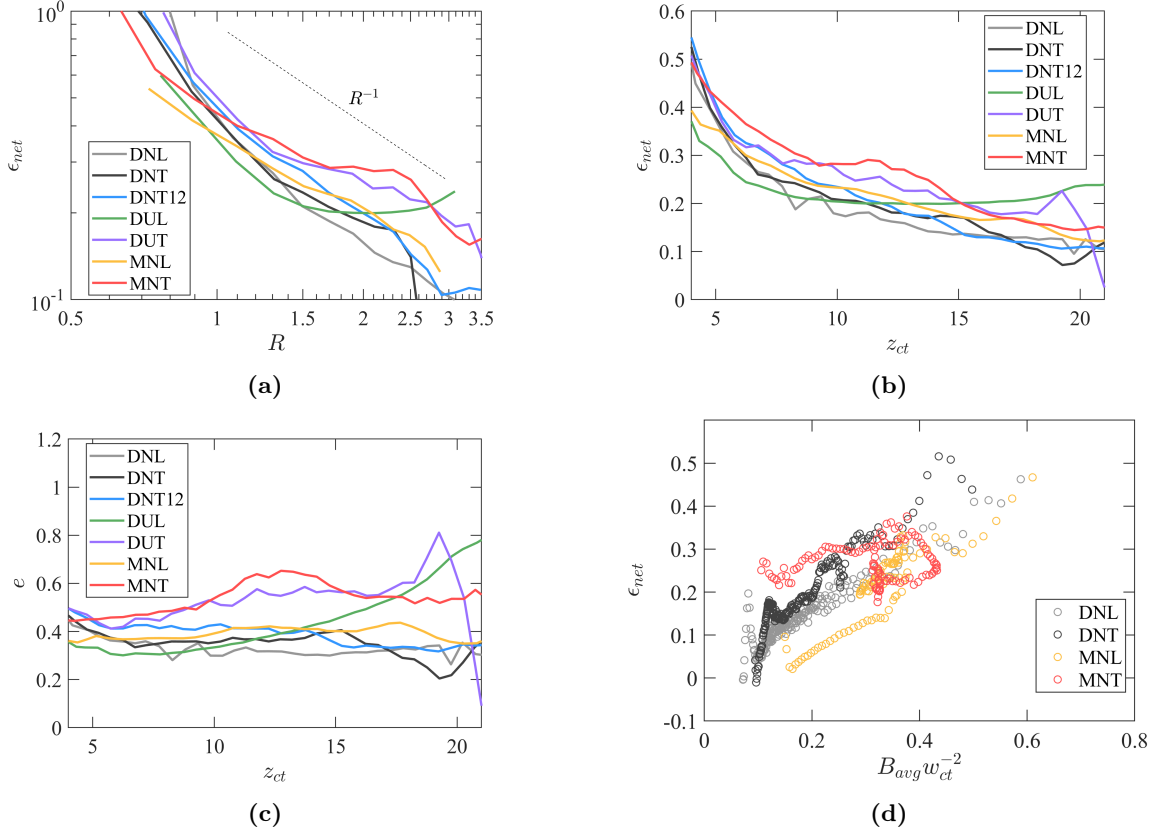


Figure 16: (a) The net entrainment rate ϵ_{net} as a function of the thermal radius R for the cases in sections IV A - IV D. The dotted line represents the scaling relation equation II.11. The moist laminar and turbulent cases seem to have slightly higher entrainment rates. (b) ϵ_{net} as a function of the thermal location z_{ct} . (c) The entrainment efficiency e (equation II.12) plotted as a function of z_{ct} . The entrainment efficiency in the moist cases is larger than the entrainment efficiency in the corresponding dry cases. (d) The correlation $\epsilon_{net} \sim B_{avg} w_{ct}^{-2}$ (see text), showing a reasonable collapse. The points are plotted for every 0.3 flow time unit

Cumulus cloud entrainment is parameterized in cloud models using dimensional and scaling relationships, with the entrainment varying as $\epsilon \propto R^{-1}$, Z_{th}^{-1} and $B_{avg} w_{th}^{-2}$ [13]. In figures 16(a,b), we plot the entrainment rate as a function of the thermal radius R and as a function of the thermal height z_{ct} . The curves deviate to different degrees from the $\epsilon_{net} \sim R^{-1}$ for dry thermals. Figure 16(a) shows that while $\epsilon_{net} \propto R^{-1}$ holds well for laminar and turbulent dry thermals, the entrainment in MNT and DUT thermals deviates from the $\epsilon_{net} \sim R^{-1}$ relationship especially in the later stages).

Both off-source addition of buoyancy to the thermals (either through condensation or through unstable stratification), while the role of turbulence (higher Re) in increasing the entrainment rate is marginal. This is seen in figure 16(c), where we plot the entrainment efficiency in these different cases.

Figure 16(c) also shows that the entrainment efficiency e in the MNL thermal is always marginally higher than the DNL thermal, consistent with the role of buoyancy in inducing entrainment envisaged in LJ19 (see also section IV A). However, this is contrary to [26] where e is lower than the dry thermal at lower levels of thermal ascent and thereafter it is similar to dry thermal. The marginal role of turbulence (alone) in entrainment is further corroborated by the observation that the entrainment at a higher (nominal) Re in the DNT12 thermal is only marginally higher than the DNT thermal. However, the entrainment in turbulent thermals with *increasing buoyancy* (MNT or DUT) is significantly higher, suggesting that the interplay of volumetric heating and turbulence is responsible. In figure 16(d), we plot the entrainment rate ϵ vs the ratio B_{avg}/w_{ct}^2 , showing that these are proportional. We note that the spread in the data is not small. A systematic study of the curves for MNT thermals as the ambient relative humidity is varied will be presented elsewhere.

For a more detailed understanding of the role of condensation heating in entrainment, we plot the entrainment and circulation terms in Eq. III.4 in Figures 17. For dry thermals, in agreement with LJ19, the circulation term remains small throughout the evolution, while the buoyancy term is balanced by the entrainment term. For both laminar and turbulent moist thermals, on the other hand, the circulation term is nonzero. As a result, the individual

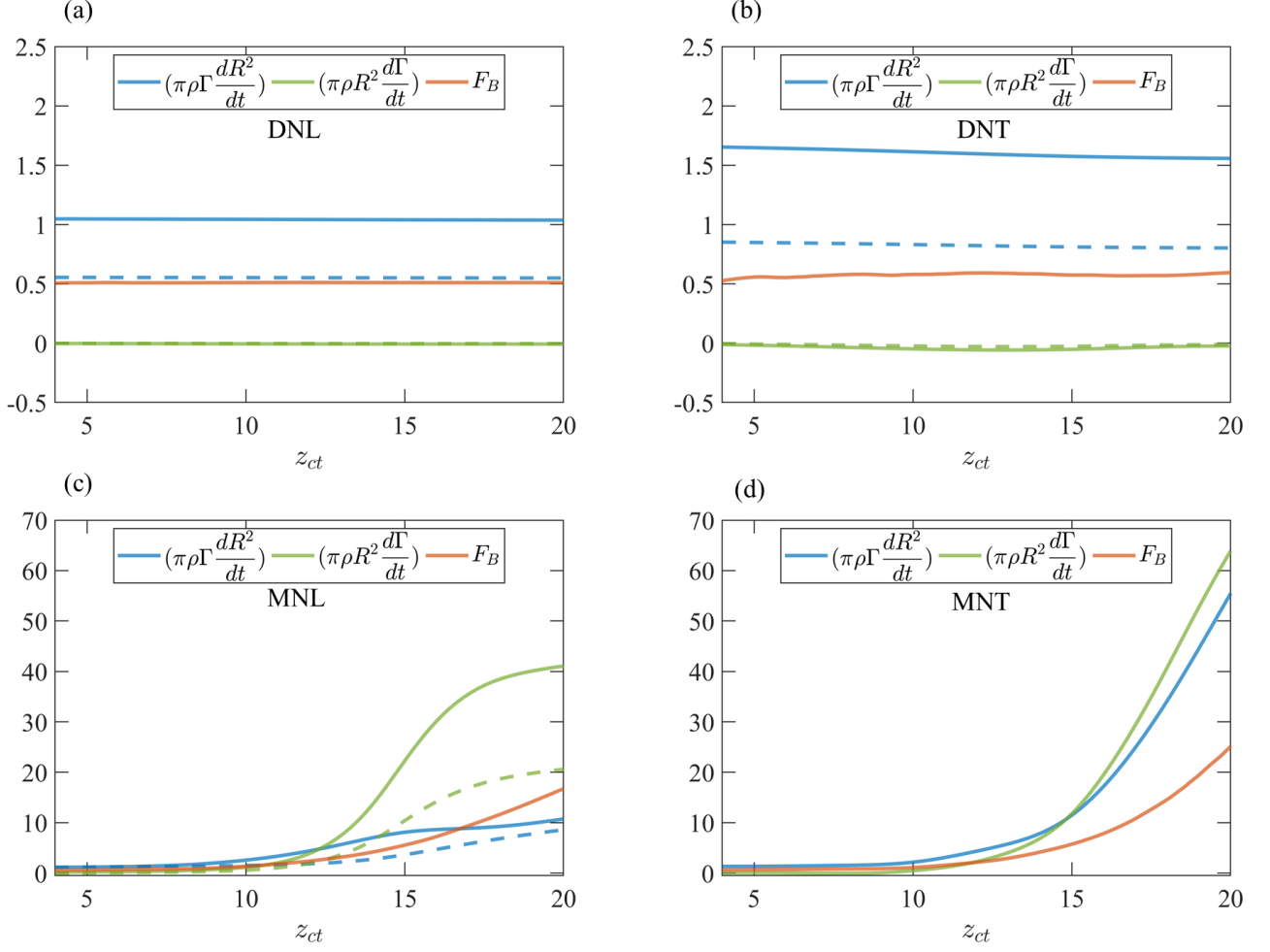


Figure 17: The terms in the impulse budget, Eq. III.4, as a function of the thermal height z_{ct} for (a) dry laminar (b) dry turbulent, (c) moist laminar and (d) moist turbulent thermals. Terms calculated using the radius of the thermal are plotted with solid lines, while terms calculated using the vortex ring radius (in plots a-c) are plotted with dashed lines. In moist thermals, the buoyancy, the circulation and entrainment terms are all an order of magnitude higher than in dry thermals. Turbulence also leads to a greater entrainment rate in moist thermals. Note that $\rho = 1$ under the Boussinesq approximation.

terms on the left hand side (LHS) of the impulse budget (Eq. III.4) in figure 17 are much larger for moist thermals than for dry thermals, and the balance implied by Eq. III.4 breaks down for moist thermals.

Furthermore, we see that the buoyancy term F_B is slightly larger for MNT than for MNL thermals. This is due to the fact that while the mean buoyancy B_{avg} in the thermals is lower for MNT thermals, the larger volume leads to a larger value of $F_B = B_{avg} \times V$. This may be seen explicitly from the plots of the average buoyancy B_{avg} in figure 18(a). We note that the mean buoyancy increases for both MNL and MNT thermals due to latent heat release by condensation, but increases much faster for MNL thermals where the entrainment is lower. In dry thermals, where there is no source of buoyancy in the flow, the buoyancy decreases as expected. Plots of the mean value C_{avg} of a passive scalar C , initialised similarly to the temperature θ and governed by the equation

$$\frac{DC}{Dt} = \frac{1}{Re} \nabla^2 C, \quad (\text{IV.1})$$

which is thus a direct measure of the dilution of the flow, also show that the larger entrainment dilutes the thermal to a greater extent, as expected.

From the foregoing arguments and figures 16–18, we draw the following conclusions about the effects of condensation heating and turbulence on entrainment: (a) an increase in buoyancy alone increases the entrainment efficiency e from 0.32 in DNL thermals to 0.39 in MNL thermals; (b) an increase in the Reynolds number alone increases

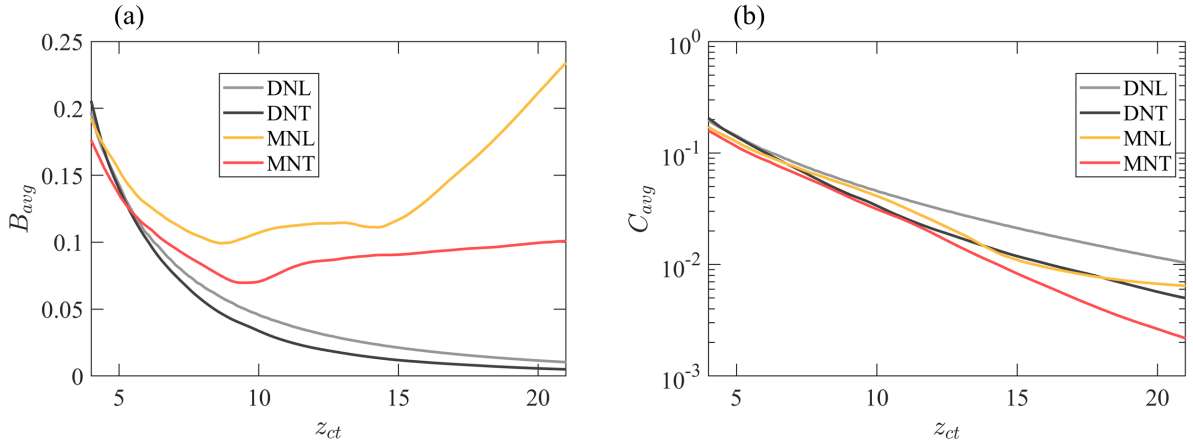


Figure 18: (a) The *average* buoyancy B_{avg} , and (b) the *average* value of the passive scalar C (see text) in dry and moist thermals as they rise in dry-neutral ambient.

e to 0.37 in DNT thermals and to a similar value in $DNT12$ thermals; (c) the combined effects of heating and turbulence lead to a significant increase in e to a value of 0.54 in MNT thermals (where the effective Reynolds number is $\approx 2 \times 10^4$.) This increase in the entrainment is made possible by the breakdown of the vortex rings, and thus equation III.4, for moist thermals. The increased entrainment is consistent with the parametric relationship $\epsilon \sim B_{avg}/w_{th}^2$, as shown in figure 16(d), because while MNT thermals have smaller average buoyancy B_{avg} , they also have smaller velocities w_{th} , than MNL thermals.

The breakdown of the vortex ring in MNT thermals is accompanied by the generation of intense small scale vorticity, as seen in figures 6 and 7(b). The role of this small-scale vorticity, which increases the mixing of the fluid inside the thermal [41], in increasing the entrainment in turbulent moist thermals merits further study.

We also note here that while we see an increase in the entrainment efficiency for moist thermals over dry thermals, laboratory experiments on dry thermals find a larger spread of entrainment values ranging from 0.4 – 0.7 [see e.g. 18, 19, 22].

V. CONCLUSION

In summary, we have presented results from direct numerical simulations (DNS) of laminar and turbulent dry thermals in neutral and unstable ambients and laminar and turbulent moist thermals in a dry-neutral ambient. Using a self-consistent and robust definition of the volume of a thermal, we studied how the properties of thermals—their velocities, volumes and radii—evolve under these different conditions. Our results for dry thermals in a neutrally stratified ambient agree with those of LJ19, and we showed that turbulence, at least for $Re \lesssim 10^4$, only causes a small increase in the entrainment rate.

We found that thermals whose buoyancy increases with time, either because of condensation heating, or because of unstable ambient stratification, entrain at *higher* rates than dry thermals in a neutral ambient, in contrast with the findings of [26], and also in contrast with some earlier numerical and experimental studies that found a decrease in entrainment upon heat addition [40, 41]. We showed that the influence of turbulence is in fact greater in these accelerating thermals, and that the change in entrainment due to the combined action of buoyancy and turbulence is greater than the change in entrainment due to either buoyancy or turbulence individually. We argued that the intense small scale vorticity generated in moist thermals and the resulting scalar mixing that occurs in the shear layers of thermals may play a role in this increase in the entrainment rate. Therefore, simulations of moist thermals at Reynolds numbers significantly higher than the mixing transition Reynolds number of $Re = 10^4$ [37] may be essential to understand the role of turbulence in cumulus entrainment.

Our results suggest several avenues for future research. The role that baroclinic torques and vorticity play in increasing the entrainment rate in moist thermals relative to dry thermals are the subject of an ongoing study. Results from such studies may be useful in devising parameterisations for the entrainment that include terms for the interaction between turbulence and volumetric heating, building on previous parameterisations of the influences of shear and baroclinic effects [48]. Furthermore, while we find that both condensation heating and unstable

stratification lead to increased entrainment, the differences between these cases (e.g. in the generation of small scale vorticity) may be studied to understand what role evaporative cooling at the edges of the thermal plays in entrainment. Such studies would build on previous studies that have addressed the role of shear turbulence in scalar mixing [44, 45].

Condensation heating, as we have seen, increases buoyancy while stable stratification would decrease buoyancy. The combined effects of condensation heating and stable stratification, therefore, would depend on the relative magnitudes of these effects. This has bearing on the transition from shallow to deep convection [e.g. 49].

Cumulus clouds are known to more closely resemble a series of thermals than steady plumes. Fully resolved studies of how ensembles of thermals interact, therefore, would help better understand how clouds behave in the Earth's atmosphere. Studies along these lines using LES have recently [15, 16] been conducted. Such studies could pave the way towards more reliable weather and climate simulations.

APPENDIX A: CALCULATION OF THERMAL VOLUME

As noted in section IIB, the volume of the thermal has to be consistently defined before the entrainment rate can be calculated. Following [10, 23, 26], we use the volume bounded by the dividing streamline $\psi = 0$ in a frame of reference moving with the thermal. This therefore requires the velocity of the thermal to first be calculated. The following are the steps involved.

(i) First, we azimuthally average the instantaneous axial and radial velocity and temperature to obtain $\bar{w}(r)$, $\bar{u}_r(r)$, and $\bar{\theta}(r)$ respectively.

(ii) These azimuthal averages are used to find the location of the centroid z_{ct} of the thermal

$$z_{ct} = \frac{\sum_{\bar{w}^* > 0.6} \bar{w}^* z}{\sum_{\bar{w}^* > 0.6} \bar{w}^*}, \quad (\text{V.1})$$

where $\bar{w}^* = \bar{w}/w_{max}$ with w_{max} the maximum flow velocity in the domain.

(iii) The velocity of the thermal is computed as

$$w_{th} = \frac{dz_{ct}}{dt},$$

where z_{ct} is computed at intervals of $\Delta t = 0.4$. As noted in [23, 50], the volume of the thermal is sensitive to the w_{th} . We therefore perform a third order Savitsa-Golay curve fit to the z_{ct} data before computing w_{th} .

(iv) The streamfunction ψ is obtained using the flow velocity in the frame of reference of the thermal, $(\bar{u}_r, \bar{w} - w_{th})$,

$$\partial_r \psi = 2\pi r(w - w_{th}) \quad \text{and} \quad \partial_z \psi = 2\pi r(u_r) \quad (\text{V.2})$$

and the dividing streamline $\psi = 0$. In some cases, the method identifies the more than one closed loop, and these have to be manually removed.

(v) The thermal volume is then given by

$$V = \int \pi r^2(z) dz$$

where the integral is calculated using composite Simpsons rule.

This method is compared with two simpler methods that only involve locating the centroid of the thermal and the top of the thermal in figure 19.

APPENDIX B: THE ROLE OF AMBIENT VAPOUR IN MOIST THERMALS

Consider a saturated parcel of air of volume $V_0 = 1$ at an altitude $z_0 = 0$ with $\theta = 0$ such that the buoyancy is $B_0 = 0$ rising adiabatically—i.e. without entrainment—to an altitude z_2 . The conservation of energy requires

$$\theta + L_2 r_s(z = 0) = L_2 = \theta(z = z_2) + L_2 r_s(z = z_2), \quad (\text{V.3})$$

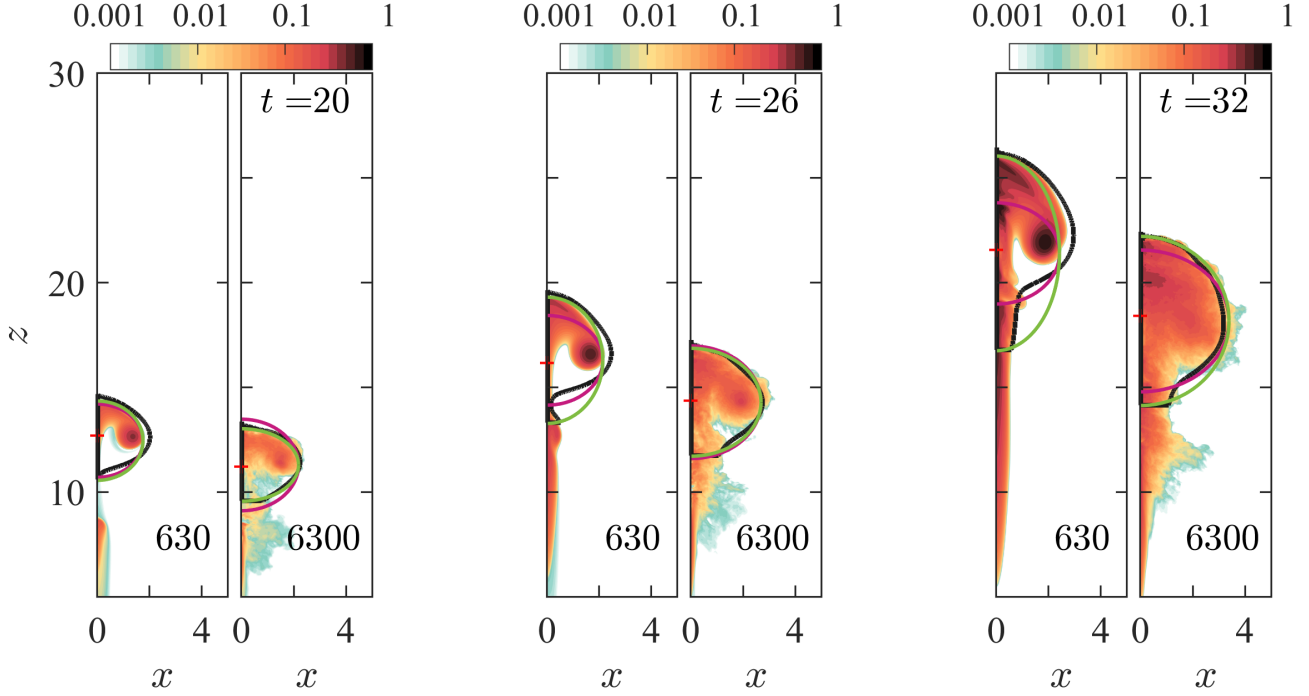


Figure 19: Identification of coherent thermals using the steps from Appendix A. The parameters are the same as in figure 8. The dividing streamline ($\psi = 0$, black curve) delineates the volume of the thermal from the ambient. The dividing streamline is superimposed on filled contours of the azimuthally averaged temperature, showing that the using the streamfunction allows for nearly autonomous boundary detection, with minimal manual intervention. The pink curve shows a spherical volume drawn with the thermal centroid as its centre and radius R (defined in section IIB). The green curve is a spheroidal volume with the distance from thermal top to the centroid as its major axis and R as its minor axis. These three methods, variously used in the literature [e.g. 12, 13, 23, 26] predict similar thermal volumes for the turbulent case while the differences are noticeable in the laminar case.

giving the adiabatic temperature $\theta_{ad} = L_2(1 - r_s(z = z_2)) \geq 0$, and the resulting buoyancy,

$$B_{ad} = (L_2 - r^0)(1 - r_s(z_2)) + r^0\chi(1 - s_\infty)r_s(z_2) \geq 0 \quad (\text{V.4})$$

Consider now a case where the parcel entrains an equal mass (or, in the Boussinesq approximation, an equal volume) of ambient air from an altitude z_1 before rising to $z = z_2$. The conservation of energy again gives

$$\theta^* + L_2r_s(z_2) = L_2 + s_\infty L_2r_s(z_1), \quad (\text{V.5})$$

giving

$$\theta^* = L_2 \left(\frac{1 + s_\infty r_s(z_1)}{2} - r_s(z_2) \right), \quad (\text{V.6})$$

and

$$B^* = (L_2 - r^0) \left[\frac{1 + s_\infty r_s(z_1)}{2} - r_s(z_2) \right] + r^0\chi[(1 - s_\infty)r_s(z_2)] \geq 0 \quad (\text{V.7})$$

The latter expressions show that for sufficiently large s_∞

1. $\theta^* \geq 0$, and thus $B^* \geq 0$; and
2. $B^* \leq B_{ad}$.

ACKNOWLEDGEMENTS

SR is supported under the Swedish Research Council grant no. 638-2013-9243. The Nordic Insitution for Theoretical Physics (Nordita) is partially supported by Nordforsk. The support and the resources provided by PARAM

Yukti Facility under the National Supercomputing Mission, Government of India at the Jawaharlal Nehru Centre for Advanced Scientific Research (JNCASR) Bangalore are gratefully acknowledged. We are grateful to Dr. Akhilesh Prabhu for discussions and help with the code, and to Prof. Rama Govindarajan for comments on the manuscript. We are grateful to the late Prof. Roddam Narasimha, for the original idea for this work.

-
- [1] C. Rio and A. D. Del Genio and F. Hourdin. Ongoing breakthroughs in convective parameterization. *Current Climate Change Reports*, 5:95–111, 6 2019.
- [2] David Randall, Marat Khairoutdinov, Akio Arakawa, and Wojciech Grabowski. Breaking the Cloud Parameterization Deadlock. *Bull. Am. Meteorol. Soc.*, 84(11):1547–1564, nov 2003.
- [3] Wojciech W. Grabowski. An improved framework for superparameterization. *Journal of the Atmospheric Sciences*, 61:1940–1952, 8 2004.
- [4] Andrew Jonjon Majda. Multiscale model with moisture and systematic strategies for superparameterization. *Journal of the Atmospheric Sciences*, 64:2726–2734, 7 2007.
- [5] Wim C. de Rooy, Peter Bechtold, Kristina Fröhlich, Cathy Hohenegger, Harm Jonker, Dmitrii Mironov, A. Pier Siebesma, Joao Teixeira, and Jun-Ichi Yano. Entrainment and detrainment in cumulus convection: an overview. *Q. J. R. Meteorol. Soc.*, 139(670):1–19, jan 2013.
- [6] Akio Arakawa. The cumulus parameterization problem: Past, present, and future. *Journal of Climate*, 17:2493–2525, 7 2004.
- [7] Ming Zhao and Philip H. Austin. Life cycle of numerically simulated shallow cumulus clouds. part i: Transport. *Journal of the Atmospheric Sciences*, 62:1269–1290, 5 2005.
- [8] Ming Zhao and Philip H. Austin. Life cycle of numerically simulated shallow cumulus clouds. part ii: Mixing dynamics. *Journal of the Atmospheric Sciences*, 62:1291–1310, 5 2005.
- [9] Rick Damiani, Gabor Vali, and Samuel Haimov. The structure of thermals in cumulus from airborne dual-doppler radar observations. *Journal of the Atmospheric Sciences*, 63:1432–1450, 5 2006.
- [10] David M. Romps and Alexander B. Charn. Sticky thermals: Evidence for a dominant balance between buoyancy and drag in cloud updrafts. *Journal of the Atmospheric Sciences*, 72:2890–2901, 8 2015.
- [11] David M. Romps and Rusen Öktem. Stereo photogrammetry reveals substantial drag on cloud thermals. *Geophysical Research Letters*, 42:5051–5057, 6 2015.
- [12] Daniel Hernandez-Deckers and Steven C. Sherwood. A numerical investigation of cumulus thermals. *Journal of the Atmospheric Sciences*, 73:4117–4136, 10 2016.
- [13] Daniel Hernandez-Deckers and Steven C. Sherwood. On the role of entrainment in the fate of cumulus thermals. *Journal of the Atmospheric Sciences*, 75:3911–3924, 11 2018.
- [14] Daniel H. Moser and Sonia Lasher-Trapp. The influence of successive thermals on entrainment and dilution in a simulated cumulus congestus. *Journal of the Atmospheric Sciences*, 74:375–392, 2 2017.
- [15] Hugh Morrison, John M. Peters, Adam C. Varble, Walter M. Hannah, and Scott E. Giangrande. Thermal chains and entrainment in cumulus updrafts. Part I: Theoretical description. *J. Atmos. Sci.*, 77(11):3637–3660, nov 2020.
- [16] John M. Peters, Hugh Morrison, Adam C. Varble, Walter M. Hannah, and Scott E. Giangrande. Thermal chains and entrainment in cumulus updrafts. part ii: Analysis of idealized simulations. *Journal of the Atmospheric Sciences*, 77:3661–3681, 11 2020.
- [17] David M. Romps, Rusen Öktem, Satoshi Endo, and Andrew M. Vogelmann. On the life cycle of a shallow cumulus cloud: Is it a bubble or plume, active or forced? *Journal of the Atmospheric Sciences*, 78:2823–2833, 9 2021.
- [18] B.R. Morton, Geoffrey Ingraham Taylor, and J. S. Turner. Turbulent gravitational convection from maintained and instantaneous sources. *Proc. R. Soc. A Math. Phys. Eng. Sci.*, 234(1196):1–23, 1956.
- [19] R. S. Scorer. Experiments on convection of isolated masses of buoyant fluid. *Journal of Fluid Mechanics*, 2:583–594, 1957.
- [20] J S Turner. The ‘starting plume’ in neutral surroundings. *J. Fluid Mech.*, 13(3):356–368, 1962.
- [21] Joanne Simpson and Viktor Wiggert. Models of precipitating cumulus towers. *Monthly Weather Review*, 97:471–489, 7 1969.
- [22] H. Johari. Mixing in thermals with and without buoyancy reversal. *Journal of the Atmospheric Sciences*, 49:1412–1426, 8 1992.
- [23] Daniel Lecoanet and Nadir Jeevanjee. Entrainment in resolved, dry thermals. *J. Atmos. Sci.*, 76(12):3785–3801, dec 2019.
- [24] Brett McKim, Nadir Jeevanjee, and Daniel Lecoanet. Buoyancy-driven entrainment in dry thermals. *Quarterly Journal of the Royal Meteorological Society*, 146:415–425, 1 2020.
- [25] David M. Romps. A Direct Measure of Entrainment. *J. Atmos. Sci.*, 67(6):1908–1927, jun 2010.
- [26] Hugh Morrison, John M. Peters, and Steven C. Sherwood. Comparing growth rates of simulated moist and dry convective thermals. *Journal of the Atmospheric Sciences*, 78:797–816, 3 2021.
- [27] E. A. Spiegel and G. Veronis. On the Boussinesq approximation for a compressible fluid. *Astrophys. J.*, 1960.
- [28] G Hernandez-Duenas, A J Majda, L M Smith, and S N Stechmann. Minimal models for precipitating turbulent convection. *J. Fluid Mech.*, 717:576–611, 2013.

- [29] S Ravichandran, Eckart Meiburg, and Rama Govindarajan. Mammatus cloud formation by settling and evaporation. *J. Fluid Mech.*, 899:A27, 2020.
- [30] I Orlanski. A simple boundary condition for unbounded hyperbolic flows. *J. Comput. Phys.*, 21(3):251–269, 1976.
- [31] S. Ravichandran and Roddam Narasimha. *arXiv preprint*, 2020.
- [32] Sourabh S. Diwan, S. Ravichandran, Rama Govindarajan, and Roddam Narasimha. Understanding transmission dynamics of covid-19-type infections by direct numerical simulations of cough/sneeze flows. *Transactions of the Indian National Academy of Engineering*, 5:255–261, 6 2020.
- [33] Rohit Singhal, S. Ravichandran, Sourabh S. Diwan, and Garry L. Brown. Reynolds stress gradient and vorticity fluxes in axisymmetric turbulent jet and plume. *Lecture Notes in Mechanical Engineering*, pages 403–411, 2021.
- [34] S. Ravichandran and Rama Govindarajan. Instability driven by settling and evaporation in a shear flow: A model for asperitas clouds. *Physical Review Fluids*, 7:010501, 1 2022.
- [35] J. S. Turner. Buoyant vortex rings. *Proceedings of the Royal Society of London. Series A. Mathematical and Physical Sciences*, 239:61–75, 2 1957.
- [36] Evan H. Anders, Daniel Lecoanet, and Benjamin P. Brown. Entropy rain: Dilution and compression of thermals in stratified domains. *The Astrophysical Journal*, 884:65, 10 2019.
- [37] P. E. Dimotakis. The mixing transition in turbulent flows. *J. Fluid Mech.*, 409:69–98, 2000.
- [38] B. Zhao, A. W. K. Law, A. C. H. Lai, and E. E. Adams. On the internal vorticity and density structures of miscible thermals. *Journal of Fluid Mechanics*, 722, 5 2013.
- [39] Roddam Narasimha. Supporting Information. *Proc. Natl. Acad. Sci. U. S. A.*, 1:6–11, 2012.
- [40] A. J. Basu and Roddam Narasimha. Direct numerical simulation of turbulent flows with cloud-like off-source heating. *J. Fluid Mech.*, 385:199–228, 1999.
- [41] G S Bhat and R Narasimha. A volumetrically heated jet: large-eddy structure and entrainment characteristics. *J. Fluid Mech.*, 325:303–330, 1996.
- [42] J. Westerweel, C. Fukushima, J. M. Pedersen, and J. C. R. Hunt. Mechanics of the turbulent-nonturbulent interface of a jet. *Physical Review Letters*, 95:174501, 10 2005.
- [43] Jimmy Philip and Ivan Marusic. Large-scale eddies and their role in entrainment in turbulent jets and wakes. *Physics of Fluids*, 24:055108, 5 2012.
- [44] M. B. Baker, R. E. Breidenthal, T. W. Choulaton, and J. Latham. The effects of turbulent mixing in clouds. *Journal of Atmospheric Sciences*, 41(2):299 – 304, 1984.
- [45] Thijs Heus and Harm J. J. Jonker. Subsiding shells around shallow cumulus clouds. *Journal of the Atmospheric Sciences*, 65:1003–1018, 3 2008.
- [46] Walter M. Hannah. Entrainment versus dilution in tropical deep convection. *J. Atmos. Sci.*, 74(11):3725–3747, nov 2017.
- [47] Hugh Morrison, John M. Peters, Adam C. Varble, Walter M. Hannah, and Scott E. Giangrande. Thermal chains and entrainment in cumulus updrafts. part i: Theoretical description. *Journal of the Atmospheric Sciences*, 77:3637–3660, 11 2020.
- [48] N B Kaye. Turbulent plumes in stratified environments: a review of recent work. *Atmosphere-ocean*, 46(4):433–441, 2008.
- [49] C M. Wu, B Stevens, and A Arakawa. What controls the transition from shallow to deep convection? *J. Atmos. Sci.*, 66(6):1793–1806, 2009.
- [50] Ari Glezer and Donald Coles. An experimental study of a turbulent vortex ring. *Journal of Fluid Mechanics*, 211:243–283, 2 1990.